# Sub-MeV Electron Precipitation Driven by EMIC waves in Plasmaspheric Plumes at High *L* shells

**Murong Qin[1], Wen Li[1], Yukitoshi Nishimura[1], Sheng Huang[1], Qianli Ma[1,2], Miroslav Hanzelka[4,5], Luisa Capannolo[1], Xiao-Chen Shen[1], Vassilis Angelopoulos[3], Xin An[3], Anton V. Artemyev[3], and Longzhi Gan[1]**

[1] Center for Space Physics, Boston University, Boston, MA, USA.

[2] Department of Atmospheric and Oceanic Sciences, University of California, Los Angeles, CA, USA.

[3] Department of Earth, Planetary, and Space Sciences, University of California, Los Angeles, CA, USA

[4] GFZ German Research Centre for Geosciences, Potsdam, Germany

[5] Department of Space Physics, Institute of Atmospheric Physics of the Czech Academy of Sciences, Prague, Czech Republic

Corresponding authors:

Murong Qin (murongqin6@gmail.com)

Wen Li (luckymoon761@gmail.com)

**Key Points:**

- EMIC-driven sub-MeV electron precipitation is observed by ELFIN, supported by conjugate THEMIS wave observations in the afternoon sector.
- Sub-MeV electron precipitation occurs at 8 < L < 10.5 in plasmaspheric plume regions, where trapped MeV electrons are nearly absent.
- Quasi-linear modeling suggests that a high $f_{pe}/f_{ce}$ ratio in plume at high *L* shells is critical for driving sub-MeV electron precipitation.

## Abstract

Electromagnetic ion cyclotron (EMIC) waves are known to be efficient for precipitating > 1 MeV electrons from the magnetosphere into the upper atmosphere. Despite considerable evidence showing that EMIC-driven electron precipitation can extend down to sub-MeV energies, the precise physical mechanism driving sub-MeV electron precipitation remains an active area of investigation. In this study, we present an electron precipitation event observed by ELFIN CubeSats on 11 January 2022, exclusively at sub-MeV energy at *L* ~ 8-10.5, where trapped MeV electrons were nearly absent. The THEMIS satellites observed conjugate H-band and He-band EMIC waves and hiss waves in plasmaspheric plumes near the magnetic equator. Quasi-linear diffusion results demonstrate that the observed He-band EMIC waves, with a high ratio of plasma to electron cyclotron frequency, can drive electron precipitation down to ~400 keV. Our findings suggest that exclusive sub-MeV precipitation (without concurrent MeV precipitation) can be associated with EMIC waves, especially in the plume region at high *L* shells.



## Plain Language Summary

Energetic electrons precipitating from the Earth's magnetosphere have a significant influence on the ionosphere and upper atmosphere, including modulating ionospheric conductance and producing aurorae. As one of the major drivers of energetic electron precipitation, EMIC waves are reported to be efficient in precipitating > 1 MeV electrons. Recently, multiple studies, including both observation and modeling, showed that electron precipitation driven by EMIC waves can also extend down to sub-MeV energies. However, the precise physical mechanism by which EMIC waves drive sub-MeV electron precipitation is still under investigation. In this study, we present a sub-MeV electron precipitation event driven by EMIC waves in plasmaspheric plumes at high *L* shells (*L* ~ 8-10.5), where trapped electrons at > 1 MeV are nearly absent. The Electron Loss and Fields INvestigation (ELFIN) CubeSats, which provide high energy and pitch angle resolution electron measurements, are utilized to identify EMIC-driven precipitation signatures. Conjugate wave and plasma measurements are obtained from the Time History of Events and Macroscale Interactions during Substorms (THEMIS) satellite near the magnetic equator. Our results demonstrate that EMIC waves in plasmaspheric plumes at high *L* shells could play an important role in driving sub-MeV electron precipitation.


## 1 Introduction

Electromagnetic ion cyclotron (EMIC) waves (0.1–10 Hz) are electromagnetic waves that typically occur in multiple distinct bands: $H^+$ band, $He^+$ band, $O^+$ band, $H^{++}$ band, $O^{++}$ band, and $N^+$ band (e.g., Anderson and Fuselier, 1993; Bashir and Ilie, 2021; Bogdanov et al., 2003; Engebretson et al., 2018; Kozyra et al., 1984; Lee et al., 2019; Usanova et al., 2024; Yu et al., 2021), with frequencies below the corresponding ion gyrofrequencies. They are typically generated by temperature anisotropy of injected ring current ions during enhanced geomagnetic activities (Fraser et al., 2010), compression of the dayside magnetosphere (Anderson and Hamilton 1993; Liu et al., 2019; Usanova et al., 2012) or through the change in the flux and pitch-angle anisotropy of the resonant ion population caused by large-amplitude ULF oscillations (Thorne et al., 2006 and references therein).

EMIC waves are known to be efficient for precipitating ~MeV electrons and producing the fast loss of radiation belt electrons (e.g., Bruno et al., 2022; Lyu et al., 2022; Mourenas et al., 2016; Qin et al., 2018, 2019, 2020, 2024; Shumko et al., 2022; Xiang et al., 2017; Zhang et al., 2016).

Meredith et al. (2003) statistically investigated the minimum resonance energy ($E_{min}$) for quasi-linear interactions between EMIC waves and electrons using Combined Release and Radiation Effects Satellite (CRRES) data and suggested that only a small fraction (~11.3%) of the observed EMIC waves can drive electron precipitation below 2 MeV. By considering the finite width of the EMIC wave frequency spectrum, Ukhorskiy et al. (2010) showed that $E_{min}$ can be as low as 400 keV, when there is sufficient wave power close to the ion gyrofrequencies. However, the appreciable wave power crossing $f_{cHe^+}$ reported by Ukhorskiy et al. (2010) requires sufficient hot $He^+$ populations. This leads to a finite wave number at ~ $f_{cHe^+}$ frequency and consequently results in an $E_{min}$ of a few MeV (Chen et al., 2011). Chen et al. (2019) conducted a 5.5-year analysis of data from the Van Allen Probes measurements and showed that only less than 1% of H-band EMIC waves can resonate with sub-MeV electrons, and none of the He-band EMIC waves can do so.

Recent studies have provided strong observational evidence that EMIC waves can precipitate electrons with energies well below 1 MeV (Capannolo et al., 2019, 2021; Hendry et al., 2017). In particular, Hendry et al., (2017) suggested that EMIC-driven electron precipitation has a peak flux predominantly at ~240 keV. Such low $E_{min}$ can be achieved through non-resonant interactions (Chen et al., 2016; An et al., 2022, 2024), nonlinear fractional resonance with oblique waves (Hanzelka et al., 2023, 2024), or a sufficiently high ratio of plasma frequency to electron gyrofrequency ($f_{pe}/f_{ce}$) through cyclotron resonant interactions (Li et al., 2007; Summers et al., 2003). Usanova et al. (2013) and Grison et al. (2021) found that EMIC wave occurrence rate in duskside plumes (12-16 MLT) increases toward the magnetopause, reaching up to ~20%. Additionally, Darrouzet et al. (2008) found that plasmaspheric plumes have a high probability of being detected in the afternoon sector (15–16 MLT) at $6 < L < 9$. Such plumes at high $L$ shells could be characterized by high values of $f_{pe}/f_{ce}$ due to their high electron density and low magnetic field strength, potentially lowering $E_{min}$, which enables EMIC waves to scatter sub-MeV electrons. Recent statistical studies have shown that while EMIC-driven precipitation events are most commonly observed from dusk to pre-midnight at $L$ ~ 5−7, a second class of events occurs at higher $L$-shells at ~7−12 (Angelopoulos et al., 2023; Capannolo et al., 2023), with $E_{min}$ decreasing as $L$ increases (Angelopoulos et al., 2023; Grach et al., 2024). Additionally, at such high $L$-shells, the trapped flux at >MeV energies is likely too low to be detected, suggesting that EMIC waves may predominantly drive only sub-MeV electron precipitation at high $L$ shells in plumes. However, despite these insights, the precise role of EMIC waves in driving sub-MeV electron precipitation at higher $L$-shells in plumes remains elusive.

In this study, we present a fortuitous case of simultaneous observations of EMIC waves and electron precipitation occurring down to ~100s of keV for five consecutive orbits in plumes at high $L$-shells. By leveraging the high-energy and pitch-angle resolution measurements from the Electron Loss and Fields INvestigation (ELFIN) mission (Angelopoulos et al., 2020) for multiple orbits at Low Earth Orbit (LEO), we identify clear EMIC-driven signatures of the observed sub-MeV electron precipitation. We conduct quasi-linear diffusion modeling to determine if EMIC waves observed by Time History of Events and Macroscale Interactions during Substorms (THEMIS) (Angelopoulos, 2008) satellites can drive the observed electron precipitation to sub-MeV energies. Finally, we quantitatively compare the modeled precipitation ratio with the observations.

## 2 Observations

### 2.1 Data

In this study, electron measurements from the ELFIN CubeSats are utilized to analyze the electron precipitation at LEO. The ELFIN mission, which consists of dual probes, was launched at an altitude of ~450 km on September 15, 2018, with an orbital period of ~1.5 hours. The electron head onboard the Energetic Particle Detector (EPD) measures electrons from ~50 keV to 6 MeV, with an energy resolution of $\Delta E/E < 40\%$. The spin axis of each CubeSat is maintained perpendicular to the orbital plane, providing full pitch-angle resolution of electrons twice per spin (~3 s). The measurements in each spin are subdivided into 16 bins, yielding a pitch-angle resolution of ~22.5$^{o}$. Such pitch-angle and energy-resolved measurements are critical for identifying the driver of energetic electron precipitation.

We also utilize conjugated measurements of waves and plasmas from THEMIS satellites located near the magnetic equator. Specifically, the Fluxgate Magnetometer (FGM) instrument (Auster et al., 2008) is used to measure low-frequency magnetic field fluctuations (up to 64 Hz). To compute the spectral density of EMIC waves, a fast Fourier transform method is applied, using a window size of 256 s and employing a shifted time window of 32 s. Additionally, the magnetic spectral density observed by the Search Coil Magnetometer (SCM) (Roux et al., 2008) is adopted to analyze whistler mode wave properties. The total electron density is inferred from the spacecraft potential (Pedersen et al., 2008) measured by the Electric Field Instrument (EFI) (Bonnell et al., 2008). The potential derived density is also compared with density measured by electrostatic analyzer (ESA) (McFadden et al., 2009).

### 2.2 Electron precipitation observed by ELFIN

Figure 1 shows an overview of sub-MeV electron precipitation observed by ELFIN. The top and middle panels in Figures 1a–e show locally trapped and precipitating electron energy fluxes, respectively. The precipitation ratios, determined by the ratios of precipitating energy flux to the locally trapped energy flux, are shown in the bottom panels of Figures 1a–e. When calculating the precipitation ratio, we removed the data with low trapped electron counts (counts < 4/s) which lead to unphysically high ratios. Both ELFIN-A and B observed electron precipitation from all five consecutive duskside orbits during the 3-hr time interval of 04:09–07:19 UT on 11 January 2022. Specifically, the intervals with electron precipitation likely driven by EMIC waves are marked by the bars with different colors in Figures 1a–1e. During these intervals, the precipitation ratio is above ~0.2 for energies ranging from ~200 keV to < 1 MeV and increases as energy increases. The latter feature suggests that the prevailing wave and plasma conditions are conducive to EMIC waves to drive the observed sub-MeV electron precipitation. This is consistent with the fact that EMIC-driven precipitation becomes progressively more efficient with increasing energy and is most effective at ~MeV energies (Angelopoulos et al., 2023; Capannolo et al., 2023). Modest precipitation was also observed for electrons below 200 keV at lower $L$ shells ($L$ < ~8), with a precipitation ratio below ~0.3, and the precipitation ratio decreases as energy increases, likely driven by whistler-mode waves (e.g., Shen et al., 2023). In this work, we mainly focus on electron precipitation associated with EMIC-driven signatures. The energy range of the EMIC-driven electron precipitation varies from orbit to orbit. For precipitation ratios >0.1, the lowest cutoff energies of electron precipitation range from 60 keV to 300 keV, and the highest cutoff energies range from ~600 keV to ~1 MeV. This feature, characterized by electron precipitation exclusively below 1 MeV, is reasonable as the trapped relativistic electron flux level >1 MeV was too low, thus little electron precipitation above 1 MeV was observed. The locations of ELFIN during observed EMIC-driven signatures are shown in Figure 1f. It is evident that electron precipitation occurs at very high $L$ shells, ranging from 8 to 10.5 on the duskside (MLT~ 16.4–17). Interestingly, the outer boundary of the precipitation moves inward over time, from $L$ ~ 10.5 at 04:12:00 UT to $L$ ~8.5 at 07:18:40 UT, suggesting the corresponding evolution of the wave-particle interaction region. It is worthwhile to note that the corresponding L-shell of the ELFIN satellites was calculated using the TS05 model (Tsyganenko & Sitnov, 2005). Fortunately, THEMIS-A, D and E were in a conjugate location with ELFIN-A in both time and space during the first orbit (Figure 1f), enabling a direct comparison between the observations of waves and electron precipitation. The THEMIS observations can also test the hypothesis that EMIC waves alone can drive the observed electron precipitation.

### 2.3 Conjugated plasma waves observed by THEMIS

The waves and plasma parameters measured by THEMIS-A, D and E near the equator are shown in Figure 2. Figures 2a and 2b show the locations of THEMIS-A (black) and ELFIN-A (blue). ELFIN-A was located at L ~ 10.7 and MLT ~ 16.4 at the time of the precipitation observation (04:12 UT). THEMIS-A was located at MLT ~15–15.5 and L ~ 9–10 when EMIC waves were observed. THEMIS-A (03:30–04:30 UT), D (02:00–03:40 UT) and E (04:10–05:00 UT) all recorded intense quasi-parallel propagating EMIC waves (Figures 2c, 2d, 2j, 2k, 2q and 2r), with intense wave power in the He-band and modest wave power in the H-band. THEMIS-A, D and E also observed whistler-mode chorus between 0.1 $f_{ce}$ and 0.5 $f_{ce}$ and broadband hiss waves (Figure 2e, 2l and 2s), with chorus waves located at lower L-shells than those of the EMIC waves. These locations are consistent with the ELFIN observations of chorus-driven electron precipitation at L < ~8 and EMIC-driven precipitation at L > ~8. Additionally, whistler-mode hiss waves occurred simultaneously with EMIC waves. The black lines in Figures 2f, 2m and 2t show the total electron density inferred from the spacecraft potential. It is evident that both EMIC waves and hiss waves intensified within the high-density plume region, where the density shows a localized increase at L~8-10. The plume region was observed shortly after the transient magnetopause crossings (L ~ 11) on the duskside, which might be associated with the enhanced convection electric field during periods of elevated geomagnetic activity (e.g., Darrouzet et al., 2008; Goldstein et al., 2004, 2014). The highest density was detected by THEMIS-A, corresponding to an exceptionally high value of $f_{pe}/f_{ce}$ of about 30 (Figure 2g). The density measured by ESA (from a few eV to ~30 keV, not shown) exhibits a similar trend to the density inferred from spacecraft potential. However, the overall electron density calculated from the ESA measurement is lower, likely because electrons with energies below a few eV are not detectable by the ESA instrument. We adopt the most intense wave power for EMIC and hiss waves (marked by two dashed vertical magenta lines) for a further analysis.

## 3 Comparison of modeled electron precipitation and observations

To evaluate whether the sub-MeV electron precipitation can be driven by the observed waves, the pitch angle scattering rates driven by He-band EMIC waves (over 03:35–04:00 UT), H-band EMIC waves (over 03:35–03:50 UT) and whistler-mode hiss waves (03:35–04:00 UT) observed by THEMIS-A were computed using the Full Diffusion Code (Ma et al., 2019, 2020, 2021; Ni et al., 2008, 2015; Qin et al., 2021, 2024). Figures 3a–3c show the corresponding bounce-averaged pitch angle diffusion coefficients ($< D_{\alpha\alpha} >$), which were calculated based on the averaged wave spectral distributions and plasma parameters measured by THEMIS-A during the above intervals. The lower (upper) cutoff frequencies are 0.27 (0.48) $f_{cH}^+$ for H-band EMIC waves and 0.53 (0.98) $f_{cHe}^+$ for He-band EMIC waves, obtained by requiring the wave intensity to be above the instrument noise level. The total electron density is derived from the spacecraft potential (Figure 2f) measured by THEMIS-A and assumed to be constant along the field lines. The corresponding value of $f_{pe}/f_{ce}$ is ~32. It is worth noting that such a high value of $f_{pe}/f_{ce}$, which can efficiently reduce the minimum resonant energy, has been rarely reported. For EMIC waves, the cyclotron harmonic resonance numbers considered in the calculation are from -5 to 5, including the Landau resonance. The waves are assumed to be quasi field-aligned at the equator, consistent with the observed wave normal angle values shown in Figure 2d, 2k and 2r, and become oblique at higher latitudes, similarly to the latitudinally-varying model by Ni et al. (2015). Cold ion compositions are assumed to be 70% for $H^+$, 20% for $He^+$, and 10% for $O^+$. The averaged wave amplitudes for H-band and He-band EMIC waves are 75 pT (over 03:35–03:50 UT) and 410 pT (over 03:35–04:00 UT), respectively. In this event, H-band EMIC waves have no contribution to electron precipitation below 10 MeV (not shown). However, He-band EMIC waves can efficiently precipitate >400 keV electrons, with bounce-averaged pitch angle diffusion coefficients ($< D_{\alpha\alpha} >$) ranging from $10^{-4}$ to $10^{-2}$ $s^{-1}$ near the loss cone (Figure 3a). This is comparable to the minimum energy of the electron precipitation observed by ELFIN (~60–300 keV) and indicates that He-band could potentially be responsible for the observed electron precipitation down to ~400 keV. The potential effects of non-linear fractional resonance (Hanzelka et al., 2023, 2024) and non-resonant scattering (An et al., 2022, 2024; Chen et al., 2016) can cause electron precipitation below the minimum resonance energy and may also account for the weak precipitation below 400 keV observed by ELFIN; however, this comparison will be a subject of future investigation. For hiss waves, 10 orders of resonant harmonics and Landau resonance are included to calculate the diffusion coefficients. The bounce-averaged diffusion coefficients show that hiss waves can scatter energetic electrons mainly below ~20 keV near the loss cone. However, they can interact with > ~100 keV electrons with equatorial pitch angle >45° and thus move the electrons towards the smaller pitch angles, where EMIC waves can take over to further precipitate the electrons into the loss cone.

Using the pitch angle diffusion coefficients at the loss cone, denoted as $< D_{\alpha\alpha} > |_{LC}$, we further quantify the electron precipitation ratio driven by He-band EMIC waves and hiss waves with the loss cone filling index, denoted as $\chi(E)$ (Ma et al., 2020; Ni et al., 2014; Shen et al., 2023). This index is defined as the ratio of electron flux just outside the loss cone to the electron flux near the center of the loss cone under the diffusion equilibrium state (Kennel and Petschek, 1966) and can be estimated as follows:

$$\chi(E) = \frac{2\int_0^1 I_0[Z_0(E)\tau]\cdot\tau\cdot d\tau}{I_0[Z_0(E)]} \quad . \tag{1}$$

Here $I_0$ is the modified Bessel function of the first kind and $Z_0 = \sqrt{\frac{D_{SD}}{(<D_{\alpha\alpha}>|_{LC})}}$, where $D_{SD}$ is the strong diffusion limit, and $\tau$ is an integration variable.

The calculated loss cone filling index is shown as the solid black line in Figure 3d, which is overall consistent with the observed precipitation ratios from ELFIN. The colored lines with error bars show the uncertainty of the measurements, determined from the standard deviation of the precipitation ratio during each interval at each energy channel. Both the observed and modeled precipitation ratios are close to 1 at energies above 500 keV and tend to decrease as energy decreases. It is also worth noting that even though the modeled electron precipitation ratio is ~1.0 for electrons above 1 MeV, no precipitation was observed at the MeV energy except during 05:45:00–05:45:39 UT (green line). This is due to the fact that there were few trapped electrons available to be precipitated at such high energy and high $L$ shells. The quantitative analysis demonstrates that the observed electron precipitation above 400 keV can be well explained by He-band EMIC waves through quasilinear theory. The modeled $E_{min}$ is ~400 keV, while the observed lowest cutoff energy where precipitation ratios are > 0.1 ranges from 60 to 300 keV. The upper bound of the observed range (300 keV) is within 25% of the modeled value, which is reasonable given the energy resolution of the instrument. However, the model does not account for precipitation in the lower energy range (60-300 keV), which warrants further investigation. We also evaluate $E_{\mathrm{min}}^*$ , which is the energy corresponding to half the peak in the measured precipitation ratio below its peak, as a proxy for the theoretical minimum resonance energy corresponding to significant wave-driven scattering toward the loss cone (Angelopoulos et al., 2023). As shown in Figure 3, most values of $E_{\mathrm{min}}^*$ (colored diamonds) range from ~300 keV to ~450 keV, which is close to the modeled result. The observed $E_{\mathrm{min}}^*$ from 05:39:06 UT to 05:39:13 UT is lower (~150 keV), potentially attributed to the spatial and temporal evolution of EMIC wave properties.

Considering the uncertainty in electron density derived from the spacecraft potential, we calculated the diffusion coefficients based on half and double values of the measured density (Figures 4a and 4b). $E_{min}$ decreases to ~100 keV with double values of the measured density and increases to ~700 keV with half values of the measured density. The corresponding loss cone filling index is shown as the dashed and dotted black lines in Figure 4c. The modeled loss cone filling index with double (half) density also agrees well with the upper (lower) boundary of the observed precipitation ratio.

As EMIC wave-driven electron precipitation may also be sensitive to cold ion compositions (Qin et al., 2019; Ross et al., 2022), we model electron precipitation under varying cold plasma compositions. Figure 5 shows the pitch angle diffusion coefficients and precipitation ratios for varying cold ion compositions, with the same density as used in Figure 3. Comparing Figure 3c to Figure 5a, it is shown that $E_{min}$ changes only slightly as the $O^+$ composition increases by 10% (from $H^+$: $He^+$: $O^+$ = 0.7:0.2:0.1 to 0.6:0.2:0.2). However, when the percentage of $He^+$ increases (Figure 5b, $H^+$: $He^+$: $O^+$ = 0.6:0.39:0.01), $E_{min}$ decreases to approximately 200 keV near the loss cone, aligning more closely with observations. Conversely, when the cold ion composition is dominated by $H^+$ (Figure 5c, $H^+$: $He^+$: $O^+$ = 0.99:0.005:0.005), $E_{min}$ increases significantly to ~2 MeV.

## 4 Summary

In this study, we report a direct observation of sub-MeV electron precipitation by the ELFIN CubeSats, characterized by an increasing precipitation ratio as a function of energy (a clear EMIC wave-driven signature) and EMIC waves observed in the conjugate equatorial region by THEMIS. In particular, EMIC waves occurred in the duskside plume at very high $L$ shells ($L$ ~ 8–10.5). The associated electron precipitation occurred primarily below 1 MeV and lasted at least for three hours.

The lowest cutoff energies of the electron precipitation range from 60 keV to 300 keV and the highest cutoff energies range from ~600 keV to ~1 MeV.

Using quasi-linear theory with cold plasma assumptions, we demonstrate that the He-band EMIC waves played a major role in driving the electron precipitation at energies above ~ 400 keV. The modeled minimum electron energy for cyclotron resonance with helium-band EMIC waves in this specific case is lower than previous modeled results obtained from quasi-linear resonance studies in the radiation belt at L < 6 (e.g., Bruno et al., 2022; Hogan et al., 2021, 2023; Qin et al., 2019; Zhang et al., 2021). For instance, Zhang et al. (2021) showed that most He-band EMIC wave-driven electron precipitation events have an $E_{\min}$ of 1.0–2.4 MeV. Capannolo et al. (2023) demonstrated that quasilinear modeling could drive EMIC-driven electron scattering down to 250 keV. However, the simulation was based on statistical observations of EMIC waves at L ~6.5, focusing exclusively on cases with wave amplitudes greater than 1 nT. Capannolo et al. (2023) also suggested that the statistical properties of EMIC waves in the simulation may differ from those driving the precipitation observed by ELFIN, emphasizing the need for one-to-one conjunction analyses to evaluate the quasi-linear effect of EMIC-driven precipitation. The $E_{\min}$ of approximately 400 keV in this case is attributed to its occurrence in the plume region at higher L-shells, where the magnetic field is weaker while the density is higher. These conditions result in high ratios of plasma to electron cyclotron frequency, which subsequently lowers $E_{\min}$. Given the fact that the occurrence of EMIC waves peaks over L ~8–10 (Grison et al., 2021; Kim et al., 2016; Usanova et al., 2013) and the high chance of detecting duskside plumes at such high *L*-shells (Darrouzet et al., 2008), our findings imply that resonant interactions with EMIC waves could potentially play an important role in sub-MeV electron precipitation, particularly when the plume region extends to very high *L*-shells.

The modeled $E_{\min}$ is approximately 400 keV, while the observed lowest cutoff energy ranges between 60 and 300 keV. The upper limit of this range (300 keV) is within 25% of the modeled value, which is a reasonable agreement considering the energy resolution of the EPD instrument. However, the model does not account for precipitation in the lower energy range (60-300 keV). This might be due to the uncertainty in the density measurement or the assumption in the cold ion composition. To address this problem, we evaluate the sensitivity of $E_{\min}$ to background electron density (Figure 4) and cold ion compositions (Figure 5) for this specific event at high *L*-shells in the plume. When the measured density is doubled, $E_{\min}$ decreases to ~100 keV, whereas halving the density increases $E_{\min}$ to ~700 keV (Figure 4). In terms of ion composition, a higher percentage of $He^+$ can efficiently decrease $E_{\min}$ to 200 keV near the loss cone, aligning more closely with observations (Figure 5b). In contrast, when the composition is dominated by $H^+$, $E_{\min}$ increases significantly (Figure 5c). The weak electron precipitation (with a precipitation ratio <0.3) below 400 keV could also be attributed to non-resonant or non-linear effects (An et al., 2022; Chen et al., 2016; Hanzelka et al., 2023, 2024), which can cause electron precipitation below the minimum resonance energy. In this case, the averaged wave amplitude is around ~410 pT, less than 1% of the background magnetic field (~50-70 nT) and is thus unlikely to drive strong non-resonant or fractionally resonant scattering. However, the peak wave power might be sufficient to cause notable non-resonant or fractionally resonant scattering. However, evaluating these effects is beyond the scope of this study and will be investigated in future research. We also evaluate $E_{min}^*$, defined as the energy at which the measured precipitation ratio reaches half its peak value below the maximum. This serves as a proxy for the theoretical minimum resonance energy corresponding to significant wave-driven scattering toward the loss-cone. Most $E_{min}^*$ values range from ~300 keV to ~450 keV, aligning more closely with the modeled results compared to the definition of cutoff energy using precipitation ratios greater than 0.1.

In summary, our findings highlight that EMIC waves can drive electron precipitation exclusively within the sub-MeV range (without MeV precipitation), particularly in the plume regions at high *L* shells, where trapped ~MeV electrons are mostly absent. Future research should focus on examining the EMIC wave properties in such regions to better understand their role in sub-MeV electron dynamics and their broader impact on magnetosphere-ionosphere coupling.

## Acknowledgments

The efforts at Boston University are supported by NASA grants of 80NSSC20K0698, 80NSSC20K1270, 80NSSC21K1312, 80NSSC23M0193, 80NSSC24K0572, 80NSSC23K0410 and 80NSSC23K1054, and NSF grants of AGS-1847818, AGS-1907698, AGS-2019950, AGS-2225445 and AGS-2247265, and AFOSR grant FA9550-23-1-0614. SH would like to acknowledge the NASA FINESST grant 80NSSC21K1385. We also acknowledge NASA award NNX14AN68G and NSF awards AGS-1242918 and AGS-2019950. THEMIS is supported by NASA NAS5-02099. MH acknowledges support from the Alexander von Humboldt Foundation.

## Open Research

Data from THEMIS mission is used for plasma and wave measurements near the equator (THEMIS team, 2008). ELFIN EPDE data are used for electron energy flux measurement (Angelopoulos et al., 2018). Data used for the figures in the manuscript are available from (Qin et al., 2025)

## References


An, X., Artemyev, A., Angelopoulos, V., Zhang, X., Mourenas, D., & Bortnik, J. (2022). Nonresonant scattering of relativistic electrons by electromagnetic ion cyclotron waves in Earth's radiation belts. Physical Review Letters, 129(13), 135101. https://doi.org/10.1103/PhysRevLett.129.135101

An, X., Artemyev, A., Angelopoulos, V., Zhang, X.-J., Mourenas, D., Bortnik, J., and Shi X. (2024). Nonresonant scattering of energetic electrons by electromagnetic ion cyclotron waves: Spacecraft observations and theoretical framework. Journal of Geophysical Research: Space Physics, 129, e2023JA031863. https://doi.org/10.1029/2023JA031863

Anderson, B. J., & Fuselier, S. A. (1993). Magnetic pulsations from 0.1 to 4.0 Hz and associated plasma properties in the Earth's subsolar magnetosheath and plasma depletion layer. Journal of Geophysical Research, 98(A2), 1461–1479. https://doi-org.ezproxy.bu.edu/10.1029/92JA02197

Anderson, B. J., and D. J. Hamilton (1993), Electromagnetic ion cyclotron waves stimulated by modest magnetospheric compressions, J. Geophys. Res., 98, 11,369–11,382, doi:10.1029/93JA00605.

Angelopoulos, V. (2008), The THEMIS mission, Space Sci. Rev., 141, 5–34, doi:10.1007/s11214-008-9336-1.

Angelopoulos, V. et al. (2018), ELFIN/EPDE, [Dataset] https://themis-data.igpp.ucla.edu/elfindata/.

Angelopoulos, V., Tsai, E., Bingley, L. et al. The ELFIN Mission. Space Sci Rev 216, 103 (2020). https://doi.org/10.1007/s11214-020-00721-7.

Angelopoulos, V., Zhang, XJ., Artemyev, A.V. et al. Energetic Electron Precipitation Driven by Electromagnetic Ion Cyclotron Waves from ELFIN's Low Altitude Perspective. Space Sci Rev 219, 37 (2023). https://doi.org/10.1007/s11214-023-00984-w.

Auster, H. U., et al. (2008), The THEMIS fluxgate magnetometer, Space Sci. Rev., 141, 235–264, doi:10.1007/s11214-008-9365-9.

Bashir, M. F., & Ilie, R. (2021). The first observation of N+ electromagnetic ion cyclotron waves. Journal of Geophysical Research: Space Physics, 126, e2020JA028716. doi:10.1029/2020JA028716

Bogdanov, A. T., Glassmeier, K.-H., Musmann, G., Dougherty, M. K., Kellock, S., Slootweg, P., & Tsurutani, B. (2003). Ion cyclotron waves in the Earth's magnetotail during CASSINI's Earth swing-by. Annals of Geophysics, 21(10), 2043–2057. doi:10.5194/angeo-21-2043-2003

Bonnell, J. W., F. S. Mozer, G. T. Delory, A. J. Hull, R. E. Ergun, C. M. Cully, V. Angelopoulos, and P. R. Harvey (2008). The Electric Field Instrument (EFI) for THEMIS, Space Sci. Rev., 141, 303–341, doi:10.1007/s11214-008-9469-2.

Bruno, A., Blum, L. W., de Nolfo, G. A., Kataoka, R., Torii, S., Greeley, A. D., et al. (2022). EMIC-wave driven electron precipitation observed by CALET on the International Space Station. Geophysical Research Letters, 49, e2021GL097529. https://doi.org/10.1029/2021GL097529

Capannolo, L., Li, W., Spence, H., Johnson, A. T., Shumko, M., Sample, J., & Klumpar, D. (2021). Energetic electron precipitation observed by FIREBIRD-II potentially driven by EMIC waves: Location, extent, and energy range from a multievent analysis. Geophysical Research Letters, 48, e2020GL091564. https://doi.org/10.1029/2020GL091564

Capannolo, L., Li, W., Ma, Q., Qin, M., Shen, X.-C., Angelopoulos, V., Artemyev, A., Zhang, X.-J., Hanzelka, M. (2023). Electron Precipitation Observed by ELFIN Using Proton Precipitation as a Proxy for Electromagnetic Ion Cyclotron (EMIC) Waves. Geophysical Research Letters, https://doi.org/10.1029/2023GL103519

Chen, L., R. M. Thorne, and J. Bortnik (2011), The controlling effect of ion temperature on EMIC wave excitation and scattering, Geophys. Res. Lett., 38, L16109, doi:10.1029/2011GL048653.

Chen, L., Thorne, R. M., Bortnik, J., and Zhang, X.-J. (2016), Nonresonant interactions of electromagnetic ion cyclotron waves with relativistic electrons, J. Geophys. Res. Space Physics, 121, 9913– 9925, doi:10.1002/2016JA022813.

Chen, L., Zhu, H., & Zhang, X. (2019). Wavenumber analysis of EMIC waves. Geophysical Research Letters, 46, 5689– 5697. https://doi.org/10.1029/2019GL082686

Darrouzet, F., De Keyser, J., Décréau, P. M. E., El Lemdani-Mazouz, F., and Vallières, X.: Statistical analysis of plasmaspheric plumes with Cluster/WHISPER observations, Ann. Geophys., 26, 2403–2417, https://doi.org/10.5194/angeo-26-2403-2008, 2008.

Engebretson, M. J., Posch, J. L., Capman, N. S. S., Campuzano, N. G., Bělik, P., Allen, R. C., et al. (2018). MMS, Van Allen Probes, GOES 13, and ground-based magnetometer observations of EMIC wave events before, during, and after a modest interplanetary shock. Journal of Geophysical Research: Space Physics, 123, 8331–8357. doi:10.1029/2018JA025984

Fraser, B. J., R. S. Grew, S. K. Morley, J. C. Green, H. J. Singer, T. M. Loto'aniu, and M. F. Thomsen (2010), Storm time observations of electromagnetic ion cyclotron waves at geosynchronous orbit: GOES results, J. Geophys. Res., 115, A05208, doi:10.1029/2009JA014516.

Grach, V. S., Artemyev, A. V., Demekhov, A. G., Zhang, X.-J., Bortnik, J., and Angelopoulos, V. (2024). Electron precipitation driven by EMIC waves: Two types of energy dispersion. Geophysical Research Letters, 51, e2023GL107604. doi:10.1029/2023GL107604

Grison, B., Santolík, O., Lukačevič, J., & Usanova, M. E. (2021). Occurrence of EMIC waves in the magnetosphere according to their distance to the magnetopause. Geophysical Research Letters, 48, e2020GL090921. https://doi.org/10.1029/2020GL090921

Hendry, A. T., Rodger, C. J., and Clilverd, M. A. (2017), Evidence of sub-MeV EMIC-driven electron precipitation, Geophys. Res. Lett., 44, 1210– 1218, doi:10.1002/2016GL071807.

Hanzelka M, Li W and Ma Q (2023), Parametric analysis of pitch angle scattering and losses of relativistic electrons by oblique EMIC waves. Front. Astron. Space Sci. 10:1163515. doi: 10.3389/fspas.2023.1163515

Hanzelka, M., Li, W., Qin, M., Capannolo, L., Shen, X., Ma, Q., et al. (2024). Sub-MeV electron precipitation driven by EMIC waves through nonlinear fractional resonances. Geophysical Research Letters, 51, e2023GL107355. https://doi.org/10.1029/2023GL107355

Hogan, B., Li, X., Zhao, H., Khoo, L., Jaynes, A., Kanekal, S., et al. (2021). Multi-MeV electron dynamics near the inner edge of the outer radiation belt. Geophysical Research Letters, 48, e2021GL095455. https://doi.org/10.1029/2021GL095455

Hogan, B., Li, X., Xiang, Z., Zhao, H., Mei, Y., O'Brien, D., et al. (2023). On the dynamics of ultrarelativistic electrons (>2 MeV) near L* = 3.5 during 8 June 2015. Journal of Geophysical Research: Space Physics, 128, e2023JA031911. https://doi.org/10.1029/2023JA031911

Kennel, C. F., and H. Petschek (1966), Limit on stably trapped particle fluxes, J. Geophys. Res., 71, 1–28.

Kim, G.-J., Kim, K.-H., Lee, D.-H., Kwon, H.-J., and Park, J.-S. (2016), Occurrence of EMIC waves and plasmaspheric plasmas derived from THEMIS observations in the outer magnetosphere: Revisit, J. Geophys. Res. Space Physics, 121, 9443– 9458, doi:10.1002/2016JA023108.

Kozyra, J. U., T. E. Cravens, A. F. Nagy, E. G. Fontheim, and R. S. B. Ong (1984), Effects of energetic heavy ions on electromagnetic ion cyclotron wave generation in the plasmapause region, J. Geophys. Res., 89(A4), 2217–2233, doi:10.1029/JA089iA04p02217.

Lee, J. H., Turner, D. L., Toledo-Redondo, S., Vines, S. K., Allen, R. C., Fuselier, S. A., et al. (2019). MMS measurements and modeling of peculiar electromagnetic ion cyclotron waves. Geophysical Research Letters, 46, 11622–11631. doi:10.1029/2019GL085182

Li, W., Y. Y. Shprits, and R. M. Thorne (2007), Dynamic evolution of energetic outer zone electrons due to wave-particle interactions during storms, J. Geophys. Res., 112, doi:10.1029/2007JA012368.

Liu, S., Xia, Z., Chen, L., Liu, Y., Liao, Z., & Zhu, H. (2019). Magnetospheric Multiscale Observation of quasiperiodic EMIC waves associated with enhanced solar wind pressure. Geophysical Research Letters, 46, 7096–7104. https://doi.org/10.1029/2019GL083421

Lyu, X., Ma, Q., Tu, W., Li, W., & Capannolo, L. (2022). Modeling the simultaneous dropout of energetic electrons and protons by EMIC wave scattering. Geophysical Research Letters, 49, e2022GL101041. https://doi.org/10.1029/2022GL101041

Meredith, N. P., R. M. Thorne, R. B. Horne, D. Summers, B. J. Fraser, and R. R. Anderson(2003), Statistical analysis of relativistic electron energies for cyclotron resonance with EMIC waves observed on CRRES, J. Geophys. Res., 108(A6), 1250, doi:10.1029/2002JA009700.

Ma, Q., Li, W., Yue, C., Thorne, R. M., Bortnik, J., Kletzing, C. A., et al. (2019). Ion heating by electromagnetic ion cyclotron waves and magnetosonic waves in the Earth's inner magnetosphere. Geophysical Research Letters, 46, 6258– 6267. https://doi.org/10.1029/2019GL083513

Ma, Q., Connor, H. K., Zhang, X.-J., Li, W., Shen, X.-C., Gillespie, D., et al. (2020). Global survey of plasma sheet electron precipitation due to whistler mode chorus waves in Earth's magnetosphere. Geophysical Research Letters, 47, e2020GL088798. https://doi.org./10.1029/2020GL088798

Ma, Q., Li, W., Zhang, X.-J., Bortnik, J., Shen, X.-C., Connor, H. K., Boyd, A. J., Kurth, W. S., Hospodarsky, G. B., Claudepierre, S. G., Reeves, G. D., & Spence, H. E. (2021). Global Survey of Electron Precipitation due to Hiss Waves in the Earth's Plasmasphere and Plumes. Journal of Geophysical Research: Space Physics, 126(8), e2021JA029644. https://doi.org/10.1029/2021JA029644

McFadden, J.P. et al. (2009). The THEMIS ESA Plasma Instrument and In-flight Calibration. In: Burch, J.L., Angelopoulos, V. (eds) The THEMIS Mission. Springer, New York, NY. https://doi.org/10.1007/978-0-387-89820-9_13

Mourenas, D., A. V. Artemyev, Q. Ma, O. V. Agapitov, and W. Li (2016), Fast dropouts of multi-MeV electrons due to combined effects of EMIC and whistler mode waves, Geophys. Res. Lett., 43, doi:10.1002/2016GL068921.

Ni, B., R. M. Thorne, Y. Y. Shprits, and J. Bortnik (2008), Resonant scattering of plasma sheet electrons by whistler-mode chorus: Contribution to diffuse auroral precipitation, Geophys. Res. Lett., 35, L11106, doi:10.1029/2008GL034032.

Ni, B., J. Bortnik, R. M. Thorne, Q. Ma, and L. Chen (2013), Resonant scattering and resultant pitch angle evolution of relativistic electrons by plasmaspheric hiss, J. Geophys. Res. Space Physics, 118, 7740–7751, doi:10.1002/2013JA019260.

Ni, B., Bortnik, J., Nishimura, Y., Thorne, R. M., Li, W., Angelopoulos, V., Ebihara, Y., & Weatherwax, A. T. (2014). Chorus wave scattering responsible for the Earth's dayside diffuse auroral precipitation: A detailed case study. Journal of Geophysical Research: Space Physics, 119, 897–908. https://doi.org/10.1002/2013JA019507

Ni, B., et al. (2015), Resonant scattering of outer zone relativistic electrons by multiband EMIC waves and resultant electron loss time scales, J. Geophys. Res. Space Physics, 120, 7357– 7373, doi:10.1002/2015JA021466.

Pedersen, A., et al. (2008), Electron density estimations derived from spacecraft potential measurements on Cluster in tenuous plasma regions, J. Geophys. Res., 113, A07S33, doi:10.1029/2007JA012636.

Qin, M., Hudson, M., Millan, R., Woodger, L., & Shekhar, S. (2018). Statistical Investigation of the Efficiency of EMIC Waves in Precipitating Relativistic Electrons. Journal of Geophysical Research: Space Physics, 123(8), 6223–6230. https://doi.org/10.1029/2018JA025419

Qin, M., Hudson, M. K., Li, Z., Millan, R. M., Shen, X.-C., Shprits, Y. Y., et al. (2019). Investigating loss of relativistic electrons associated with EMIC waves at low L values on 22 June 2015. Journal of Geophysical Research: Space Physics, 124, 4022–4036. https://doi.org/10.1029/2018JA025726

Qin, M., Hudson, M., Millan, R., Woodger, L., & Shen, X. (2020). Statistical dependence of EMIC wave scattering on wave and plasma parameters. Journal of Geophysical Research: Space Physics, 125, e2020JA027772. https://doi.org/10.1029/2020JA027772

Qin, M., Li, W., Ma, Q., Woodger, L., Millan, R., Shen, X.-C., & Capannolo, L. (2021). Multi-Point Observations of Modulated Whistler-Mode Waves and Energetic Electron Precipitation. Journal of Geophysical Research: Space Physics, 126(12), e2021JA029505. https://doi.org/10.1029/2021JA029505

Qin M, Li W, Ma Q, Shen X-C, Woodger L, Millan R and Angelopoulos V (2024a) Large-scale magnetic field oscillations and their effects on modulating energetic electron precipitation. Front. Astron. Space Sci. 11:1253668. doi: 10.3389/fspas.2024.1253668.

Qin, M., Li, W., Shen, X.-C., Angelopoulos, V., Selesnick, R., Capannolo, L., et al. (2024b). Global survey of energetic electron precipitation at low Earth orbit observed by

ELFIN. Geophysical Research Letters, 51, e2023GL105134. https://doi.org/10.1029/2023GL105134

Qin, M., Li, W., et al. (2025), Dataset for Sub-MeV Electron Precipitation Driven by EMIC waves in Plasmaspheric Plumes at High L shells, [Dataset] https://figshare.com/s/3ba1a0c2420eb0faeedc.

Ross, J. P. J., Glauert, S. A., Horne, R. B., & Meredith, N. P. (2022). The importance of ion composition for radiation belt modeling. Journal of Geophysical Research: Space Physics, 127, e2022JA030680. https://doi.org/10.1029/2022JA030680

Roux, A., Le Contel, O., Coillot, C. et al. The Search Coil Magnetometer for THEMIS. Space Sci Rev 141, 265–275 (2008). https://doi.org/10.1007/s11214-008-9455-8

Shen, X.-C., Li, W., Capannolo, L., Ma, Q., Qin, M., Artemyev, A. V., et al. (2023). Modulation of energetic electron precipitation driven by three types of whistler mode waves. Geophysical Research Letters, 50, e2022GL101682. http://doi.org/10.1029/2022GL101682

Shumko, M., Gallardo-Lacourt, B., Halford, A. J., Blum, L. W., Liang, J., Miyoshi, Y., et al. (2022). Proton aurora and relativistic electron microbursts scattered by electromagnetic ion cyclotron waves. Frontiers in Astronomy and Space Sciences, 9. https://doi.org/10.3389/fspas.2022.975123

Summers, D., Ni, B., & Meredith, N. P. (2007). Timescales for radiation belt electron acceleration and loss due to resonant wave-particle interactions: 2. Evaluation for VLF chorus, ELF hiss, and electromagnetic ion cyclotron waves: RADIATION BELT ELECTRON TIMESCALES. Journal of Geophysical Research: Space Physics, 112(A4), https://doi.org/10.1029/2006JA011993.

THEMIS team. (2008), THEMIS, [Dataset] http://themis.ssl.berkeley.edu/data/themis.

Thorne, R.M., Horne, R.B., Jordanova, V.K., Bortnik, J. and Glauert, S. (2006). Interaction of Emic Waves With Thermal Plasma and Radiation Belt Particles. In Magnetospheric ULF Waves: Synthesis and New Directions (eds K. Takahashi, P.J. Chi, R.E. Denton and R.L. Lysak). https://doi.org/10.1029/169GM14

Ukhorskiy, A. Y., Shprits, Y. Y., Anderson, B. J., Takahashi, K., and Thorne, R. M. (2010), Rapid scattering of radiation belt electrons by storm-time EMIC waves, Geophys. Res. Lett., 37, L09101, doi:10.1029/2010GL042906.

Usanova, M. E., Mann, I. R., Bortnik, J., Shao, L., and Angelopoulos, V. (2012), THEMIS observations of electromagnetic ion cyclotron wave occurrence: Dependence on AE, SYMH, and solar wind dynamic pressure, J. Geophys. Res., 117, A10218, doi:10.1029/2012JA018049.

Usanova, M. E., Darrouzet, F., Mann, I. R., and Bortnik, J. (2013), Statistical analysis of EMIC waves in plasmaspheric plumes from Cluster observations, J. Geophys. Res. Space Physics, 118, 4946– 4951, doi:10.1002/jgra.50464.

Usanova, M. E., Woodger, L. A., Blum, L. W., Ergun, R. E., Girard, C., Gallagher, D. L., et al. (2024). H+, He+, He++, O++, N+ EMIC wave occurrence and its dependence on geomagnetic conditions: Results from 7 years of Van Allen Probes observations. Journal of Geophysical Research: Space Physics, 129, e2024JA032627. https://doi.org/10.1029/2024JA032627

Xiang, Z., Tu, W., Li, X., Ni, B., Morley, S. K., & Baker, D. N. (2017). Understanding the mechanisms of radiation belt dropouts observed by Van Allen Probes. Journal of Geophysical Research: Space Physics, 122, 9858–9879. https://doi.org/10.1002/2017JA024487

Yu, X., Yuan, Z., & Ouyang, Z. (2021). First observations of O2+ band EMIC waves in the terrestrial magnetosphere. Geophysical Research Letters, 48, e2021GL094681. doi:10.1029/2021GL094681

Zhang, X.-J., et al. (2016), Direct evidence for EMIC wave scattering of relativistic electrons in space, J. Geophys. Res. Space Physics, 121, 6620–6631, doi:10.1002/2016JA022521.

Zhang, X.-J., Mourenas, D., Shen, X.-C., Qin, M., Artemyev, A. V., Ma, Q., Li, W., Hudson, M. K., & Angelopoulos, V. (2021). Dependence of Relativistic Electron Precipitation in the Ionosphere on EMIC Wave Minimum Resonant Energy at the Conjugate Equator. Journal of Geophysical Research: Space Physics, 126(5), e2021JA029193. https://doi.org/10.1029/2021JA029193

## Figures and Captions

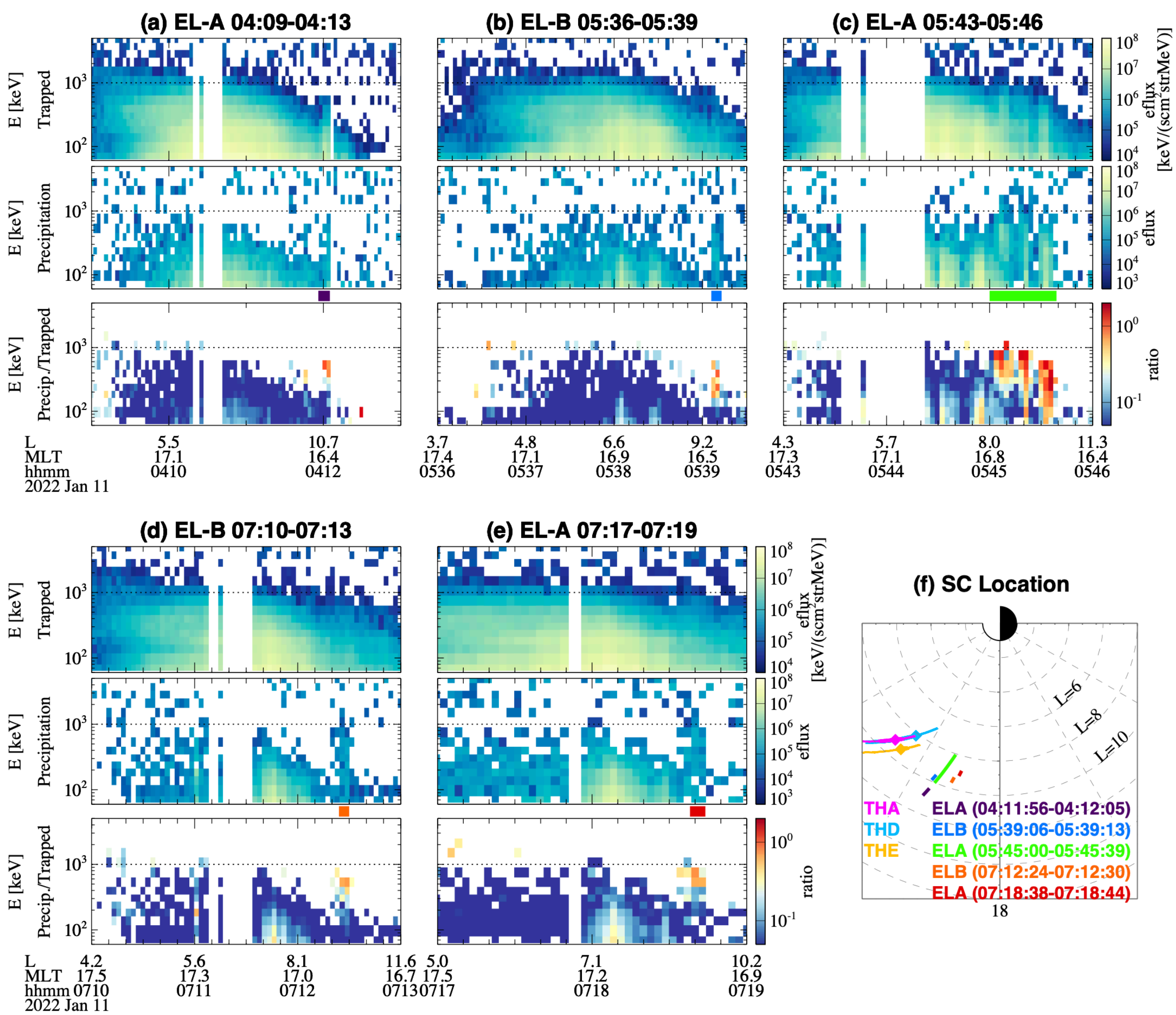


**Figure 1**. Overview of ELFIN-A and B observations during five consecutive orbits on 11 January 2022. The top, middle, bottom panels in panels (a-e) show trapped electron energy fluxes,

precipitating electron energy fluxes and the precipitating-to-trapped ratio, respectively. The dashed horizontal black lines in panels (a-e) show the 1 MeV energy. The color bars above the precipitation ratio panels show the intervals with EMIC-driven signatures. Panel (f) shows the *L*-MLT locations of the ELFIN CubeSats during the observed precipitation intervals (color bars) and the THEMIS satellites in the conjugate locations. Superimposed thicker lines on the trajectories of THEMIS represent the intervals when EMIC waves were observed. Diamonds represent the location of THEMIS when electron precipitation was observed.

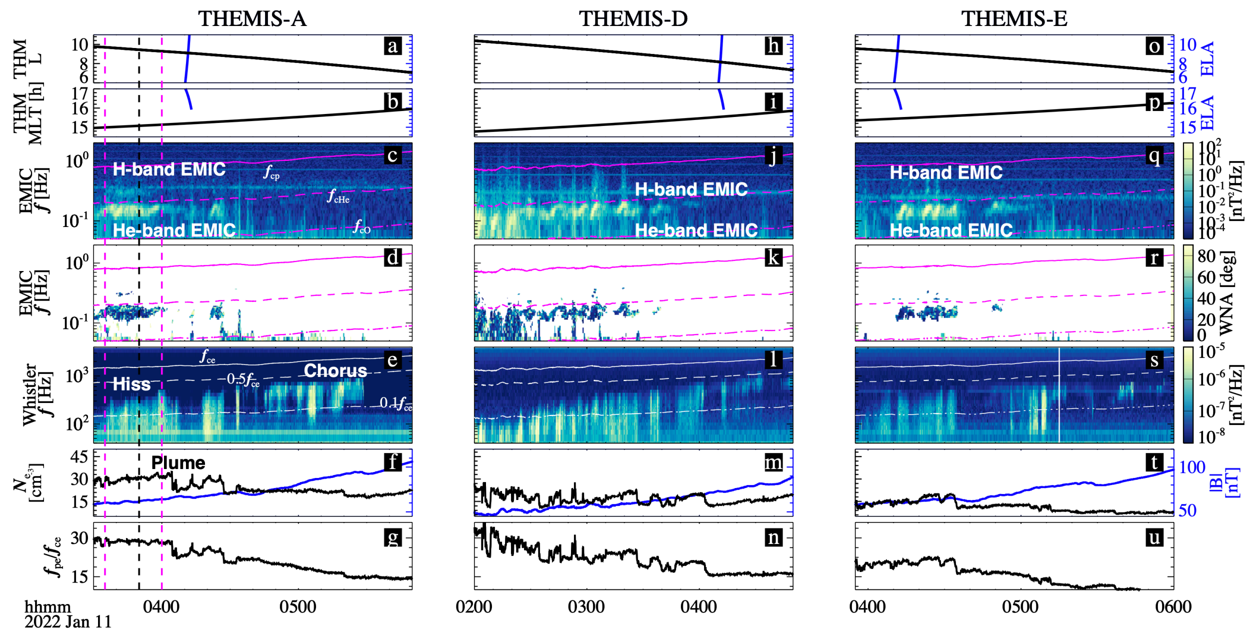


**Figure 2.** Overview of the waves and background plasma conditions observed by THEMIS-A (left), D (middle) and E (right). (a) L-shell and (b) MLT of THEMIS (black lines) and ELFIN-A (blue lines) based on the TS05 magnetic field model; (c) magnetic spectral density over 0.02–2 Hz, where the white lines represent proton, helium, and oxygen cyclotron frequencies; (d) EMIC wave normal angles; (e) magnetic spectral density over 40–4000 Hz, where the white lines represent the electron gyrofrequency ($f_{ce}$, solid), 0.5 $f_{ce}$ (dashed) and 0.1 $f_{ce}$ (dotted); (f) total electron density (black line) inferred from the spacecraft potential (Pedersen et al., 2008) and local magnetic field intensity (blue lines); (g) ratio of plasma frequency to electron gyrofrequency ($f_{pe}/f_{ce}$). The interval between the two dashed magenta lines is adopted to calculate the quasi-linear diffusion coefficients of He-band EMIC waves and hiss waves. The interval between the first magenta line and the dashed black line is adopted to calculate the quasi-linear diffusion coefficients of H-band EMIC waves. Panels (h)–(n) and (o)–(u) have the same format as panels (a)–(g), but observed by THEMIS-D and THEMIS-E, respectively.

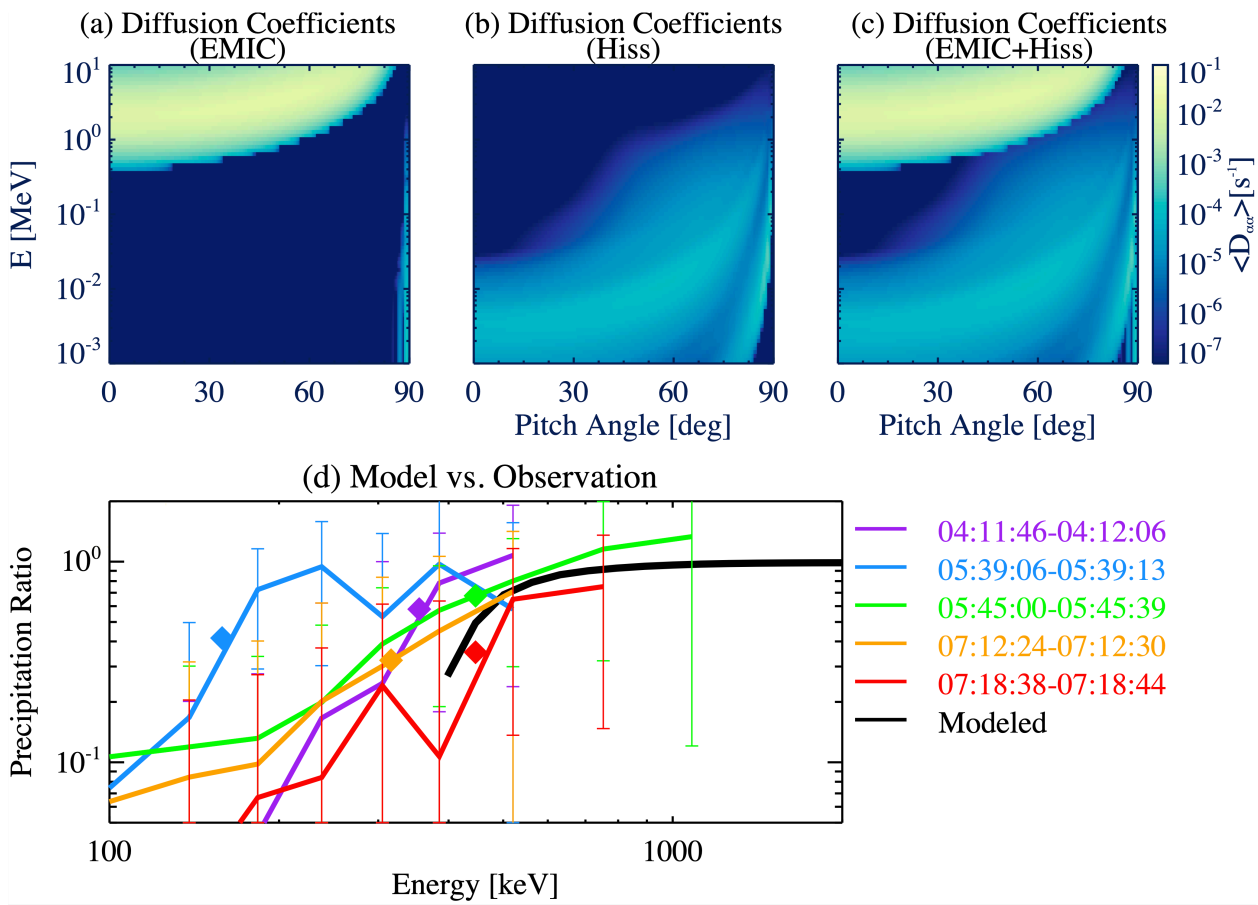


**Figure 3.** Quasi-linear modeling of electron precipitation driven by EMIC waves and hiss waves observed by THEMIS-A. (a-c) Drift- and bounce-averaged pitch angle diffusion coefficients as a function of pitch angle and energy for (a) He-band EMIC waves (03:35-04:00 UT), (b) plume hiss waves (03:35-04:00 UT); (c) combined diffusion coefficients for He-band EMIC waves and hiss waves; (d) Comparison of the modeled precipitation ratio (loss cone filling index marked by the black lines) and the ELFIN observed electron precipitation ratio (purple, blue, green, orange and red lines) corresponding to the intervals with the labeled color bars shown in Figure 1. The black lines represent the modeled result with 1 (solid), 2 (dashed) and 0.5 (dotted) times of the measured electron density from THEMIS-A. The colored diamonds represent $E^*_{\min}$, at which the measured precipitation ratio reaches half its peak value below the maximum. The colored error bars represent the mean error in determining the precipitation ratio from trapped and precipitating electron counts within the given period.

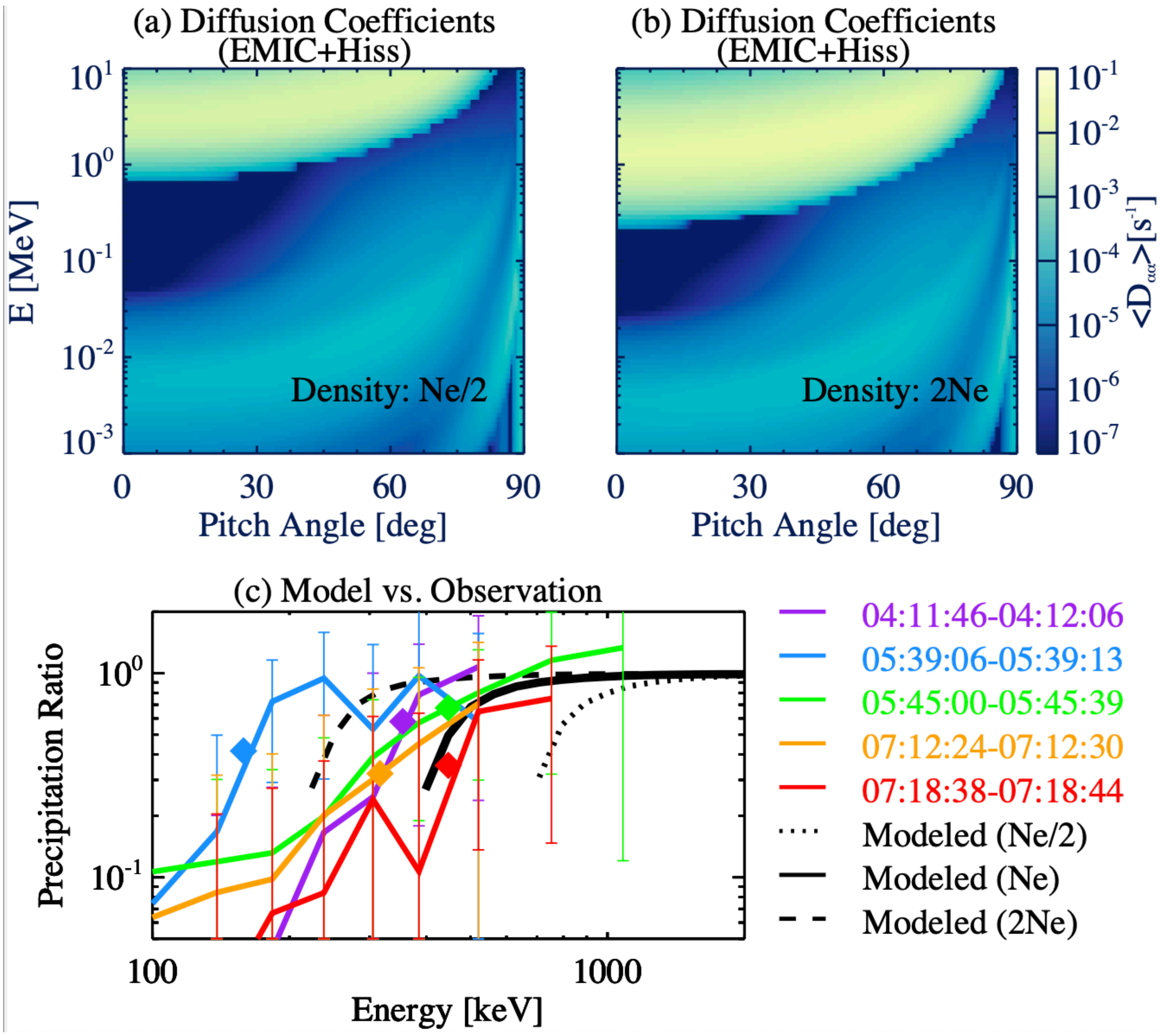


**Figure 4.** Quasi-linear modeling of electron precipitation driven by EMIC waves and hiss waves observed by THEMIS-A with various electron densities. The combined drift- and bounce-averaged pitch angle diffusion coefficients for He-band EMIC waves and hiss waves as a function of pitch angle and energy with the background electron density of (a) half and (b) double the measured density. (c) Similar to Figure 3d, except for the two additional black lines representing modeled precipitation ratio with 2 (dashed black line) and 0.5 (dotted black line) times the measured electron density from THEMIS-A.

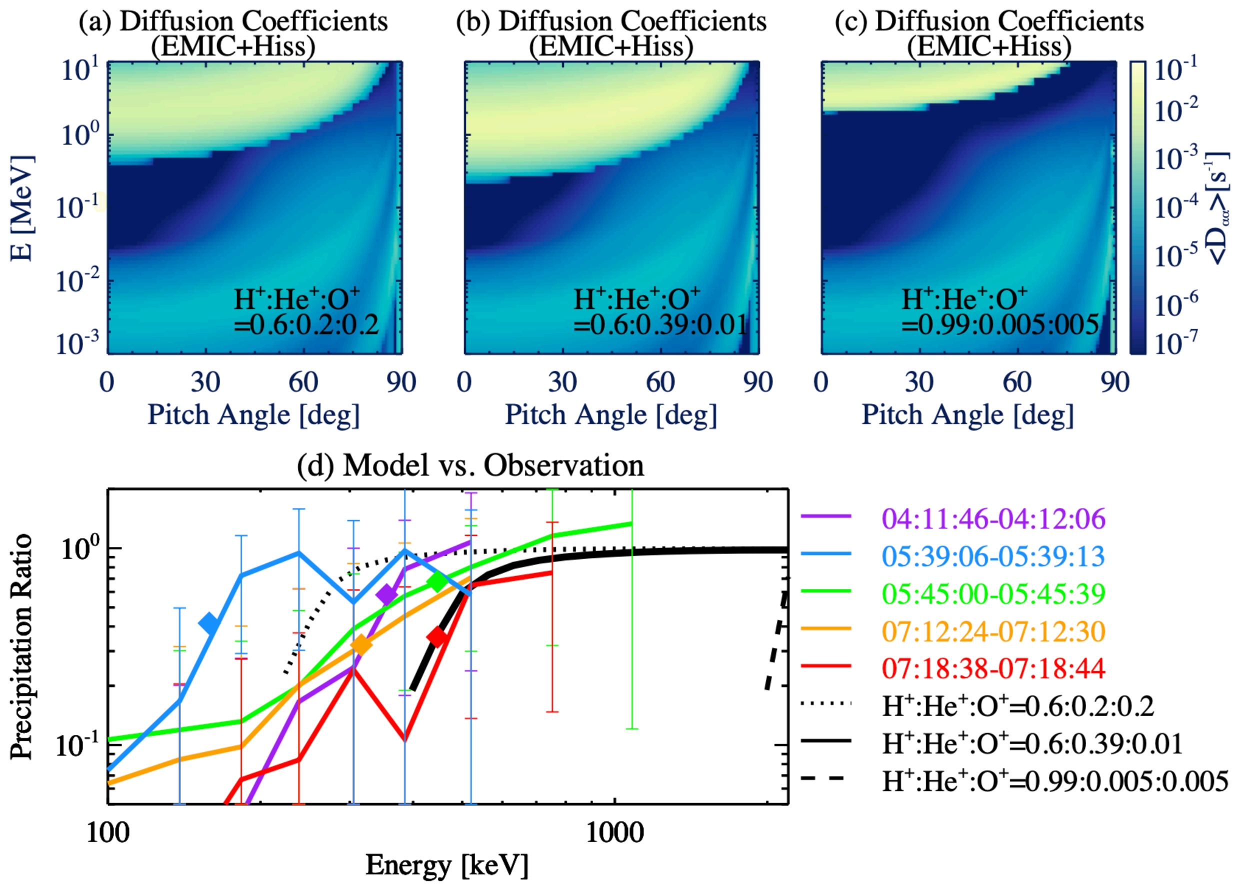


**Figure 5.** Quasi-linear modeling of electron precipitation driven by EMIC waves and hiss waves observed by THEMIS-A with various cold ion compositions. (a-c) Drift- and bounce-averaged pitch angle diffusion coefficients as a function of pitch angle and energy for cold ion composition $H^+$: $He^+$: $O^+$ of (a) 0.6:0.2:0.2; (b) 0.8:0.1:0.1; (c) 0.99:0.005:0.005. (d) Similar to Figure 3d, except for the three black lines representing modeled precipitation ratios with cold ion compositions $H^+$: $He^+$: $O^+$ of 0.6:0.2:0.2 (dotted), 0.6:0.39:0.01(solid) and 0.99:0.005:0.005 (dashed), respectively.